



Impact of the Core Deformation on the Tidal Heating and Flow in Enceladus' Subsurface Ocean

 Burak Aygün¹  and Ondřej Čadek¹ 
¹Department of Geophysics, Faculty of Mathematics and Physics, Charles University, Prague, Czech Republic

Key Points:

- The heat production in the ocean depends on the ocean thickness and the material properties of the core
- Dissipation is likely to be negligible for ocean thicknesses >1 km but can exceed 20 GW if the ocean is thin and the core is easy to deform
- The shallow water approach, widely used in previous studies, can lead to incorrect results regardless of ocean thickness

Supporting Information:

Supporting Information may be found in the online version of this article.

Correspondence to:

 B. Aygün,
aygun@karel.troja.mff.cuni.cz

Citation:

 Aygün, B., & Čadek, O. (2023). Impact of the core deformation on the tidal heating and flow in Enceladus' subsurface ocean. *Journal of Geophysical Research: Planets*, 128, e2023JE007907. <https://doi.org/10.1029/2023JE007907>

Received 12 MAY 2023

Accepted 2 NOV 2023

Author Contributions:

Conceptualization: Burak Aygün, Ondřej Čadek

Methodology: Burak Aygün, Ondřej Čadek

Software: Burak Aygün

Validation: Burak Aygün

Visualization: Burak Aygün

Abstract We present a novel approach to modeling the tidal response of icy moons with subsurface oceans. The problem is solved in the time domain and the flow in the ocean is calculated simultaneously with the deformation of the core and the ice shell. To simplify the calculations, we assume that the internal density interfaces are spherical and the effective viscosity of water is equal to or greater than 100 Pa s. The method is used to study the effect of an unconsolidated core on tidal dissipation in Enceladus' ocean. We show that the partitioning of tidal heating between the core and the ocean strongly depends on the thickness of the ocean layer. If the ocean thickness is significantly greater than 1 km, heat production is dominated by tidal dissipation in the core and the amount of heat produced in the ocean is negligible. In contrast, when the ocean thickness is less than about 1 km, tidal heating in the core diminishes and dissipation in the ocean increases, leaving the total heat production unchanged. Extrapolation of our results to realistic conditions indicates that tidal flow is turbulent which suggests that the linearized Navier-Stokes equation may not be appropriate for modeling the tidal response of icy moons. Finally, we compare our results with those obtained by solving the Laplace tidal equations and discuss the limitations of the two-dimensional models of ocean circulation.

Plain Language Summary The origin of the heat powering Enceladus' geological activity and preventing its ocean from freezing has been debated since the discovery of a plume of icy particles above Enceladus' south pole in 2005. Here, we evaluate the heat generated by tides in Enceladus' ocean assuming that the internal density interfaces are spherical and the flow in the ocean is primarily driven by the deformation of Enceladus' unconsolidated core. We find that the heat production in the ocean can explain only a small fraction of Enceladus' heat budget under the present day conditions (i.e., for an ocean thickness of about 40 km) but can be as high as 25 GW if the thickness of the ocean layer is less than about 1 km. Analysis of the flow field suggests that the simplifying assumptions often used in previous studies may not be appropriate. In particular, we show that, regardless of ocean thickness, the dissipation rate obtained by solving the shallow water equations corrected for the dampening effect of the ice shell can be significantly different from that obtained by solving the three-dimensional Navier-Stokes equations.

1. Introduction

Enceladus is a small icy moon with a global subsurface ocean. The ocean is likely to be maintained by tidal dissipation but the data tell us little about how and where the dissipation takes place. The total internal power of Enceladus is estimated to be between 10 and 50 GW (for a review, see Nimmo et al. (2018)). Analysis of the stability of the ice shell suggests that the viscosity of ice at the contact with the ocean is higher than 3×10^{14} Pa s (Čadek et al., 2019b). If this estimate is correct, then the heating rate due to tidal dissipation in the ice shell is ~ 1 GW (Souček et al., 2019), which is much less than the heat loss due to conduction (≈ 40 GW, Čadek et al., 2019b). This indicates that the heat necessary to maintain the ocean at the melting temperature is produced in the core or the ocean itself.

Since the interior of Enceladus is likely to have never been exposed to high temperatures and pressures, the core may be made of unconsolidated, easily deformable, porous rock (Roberts, 2015; Travis & Schubert, 2015). Tidal deformation of such a material is associated with rearrangements of rock fragments, producing frictional heat that may explain Enceladus' heat budget (Choblet et al., 2017; Rovira-Navarro et al., 2022).

The amount of tidal heat generated within the ocean is still debated. The prevailing view is that heating caused by ocean tides is negligible at present but may have been significant in the past when dissipation could have been enhanced by resonance effects and/or the thickness of the ocean was strongly reduced (e.g., Hay & Matsuyama, 2019; Matsuyama et al., 2018). In addition to tides, dissipation in the ocean can be caused by the

© 2023 The Authors.

This is an open access article under the terms of the Creative Commons Attribution-NonCommercial License, which permits use, distribution and reproduction in any medium, provided the original work is properly cited and is not used for commercial purposes.

turbulent flow response to the longitudinal libration of the ice shell. Whether this mechanism can provide enough heat to explain Enceladus' heat production, as suggested by, for example, Lemasquier et al. (2017) and Wilson and Kerswell (2018), will require further examination.

The first models of tidal dissipation in a subsurface ocean were based on the solution of the Laplace tidal equations (LTE). The studies pointed out the possible role of inertial waves in the thermal evolution of icy moons (Tyler, 2008, 2009, 2014, 2020) and provided the first estimates of the dissipative heat generated by oceans on Enceladus, Europa and other icy satellites (Chen et al., 2014; Hay & Matsuyama, 2017; Matsuyama, 2014). The limitation of this approach was that it was based on two simplifying assumptions: First, the thickness of the ocean, D , was assumed to be small compared to the outer radius of the ocean, R_{io} , and second, the upper surface of the ocean was assumed to be free to move. In reality, neither of these assumptions is true: The ocean on Enceladus is not shallow ($D/R_{io} \approx 0.15$, see, e.g., Čadek et al. (2016), Beuthe et al. (2016) or Hemingway and Mittal (2019)) and its surface is covered with a 20–25 km thick layer of solid ice (Thomas et al., 2016). Beuthe (2016) showed that the ice shell has a strong stabilizing effect on the tidal flow in the ocean, leading to a significant reduction of tidal dissipation. In the years that followed, the approach based on the solution of LTE, but including the dampening effect of the ice shell, was used to obtain more accurate estimates of dissipative power generated by subsurface oceans (Hay et al., 2020; Matsuyama et al., 2018) and to study the impact of non-linear bottom drag and ocean thickness variations on tidal dissipation (Hay & Matsuyama, 2019; Rovira-Navarro et al., 2020).

To date, there are only two studies (Rekier et al., 2019; Rovira-Navarro et al., 2019) that have examined the tidal dissipation in a subsurface ocean by solving the three-dimensional Navier-Stokes equation (NSE). In both studies, the non-linear term in NSE ($\boldsymbol{v} \cdot \nabla \boldsymbol{v}$ where \boldsymbol{v} is the flow velocity) is neglected and the problem is transformed into the frequency domain. The deformation of the ice shell is assumed not to be affected by the flow of water and is imposed as a boundary condition at the surface of the ocean. The former study also takes into account the deformation of the core and includes the effects of self-gravitation and libration. The studies carefully analyze the role of inertial modes and agree that the heat production in Enceladus' present-day ocean is much smaller than the heat flux observed by Cassini (Spencer et al., 2018).

This paper offers an alternative approach to modeling the tidal response of a planetary body with a subsurface ocean. The approach is different from that used by Rovira-Navarro et al. (2019) and Rekier et al. (2019) in two respects: First, the tidal response is evaluated not only in the ocean but also in the crust and the core. In our approach, the equations governing the deformation in different parts of the body are linked by the boundary conditions guaranteeing the continuity of the velocity and traction vectors. This allows us to assess the effect of mechanical and gravitational coupling between the layers on the tidal dissipation process and specifically to investigate the interaction between the ocean and Enceladus' weak core. Second, the problem of tidal deformation is solved directly in the time domain as an initial value problem, similarly as in the case of thermal convection (except that the buoyancy force is replaced by the tidal force, see, e.g., Appendix A in Kverka and Čadek (2022)). Although this approach is computationally more demanding than the solution in the frequency domain, it makes it possible to assess, at least in principle, the relative importance of non-linear effects and resonant interactions. These effects cannot be investigated by standard frequency domain methods because the response of a non-linear system to a periodic loading is not necessarily periodic in time. Our approach is also more general than that of Beuthe (2016) and Matsuyama et al. (2018) who coupled the flow in the ocean with the deformation of the ice shell and the core but used the LTE to calculate the tidal response of the ocean.

Modeling the coupled tidal deformation of an icy moon with a subsurface ocean and a plastic core is challenging and, therefore, several simplifying assumptions have been made to make the problem more amenable to solution. The most important one is the assumption that the lower boundary of the ice shell is spherical. This assumption is motivated by numerical convenience and is widely used in studies of subsurface ocean dynamics that employ numerical tools based on the spectral decomposition of the governing equations. While the assumption of a constant ice shell thickness may be approximately satisfied in the case of large, slowly rotating icy moons, such as Titan, it is not valid for Enceladus where the thickness of ice varies laterally by tens of kilometers (e.g., Beuthe et al., 2016; Čadek et al., 2016, 2019b; Hemingway & Mittal, 2019; Hoolst et al., 2016). Although these variations are likely to affect the flow in the ocean (Kang et al., 2022; Rovira-Navarro et al., 2020, 2023; Soderlund et al., 2020), most studies addressing Enceladus' ocean dynamics do not include them because of the numerical difficulties arising from the implementation of irregular boundaries in spectral methods (e.g., Beuthe, 2016; Matsuyama et al., 2018; Rekier et al., 2019; Rovira-Navarro et al., 2019; Soderlund, 2019). One

way to solve problems with complex geometry is to use the finite element method. However, even though this method has proven to be effective in modeling the tidal deformation and viscous flow in Enceladus' ice shell (Běhounková et al., 2017; Berne et al., 2023; Čadek et al., 2019a, 2019b; Souček et al., 2016, 2019), its application to the tides in the ocean is still prohibitively expensive due to the fact that the thickness of the boundary layers in the ocean is much smaller than the characteristic length scale in the ice shell and, therefore, simulations have to be performed with a spatial resolution that is significantly higher than that usually considered in the ice shell.

Another limitation of our approach is that the viscosity of water used in our model is likely to be higher than the effective viscosity in the real ocean. The lowest value of the dynamic viscosity, η , that can be achieved in our numerical simulations is 100 Pa s, which is five orders of magnitude more than the molecular viscosity of water. Time-domain simulations with $\eta < 100$ Pa s place extreme demands on the numerical resolution needed to represent the velocity field and will require algorithms that achieve a higher level of parallelization and memory management. The lowest viscosity used in the 3D frequency domain simulations by Rovira-Navarro et al. (2019) and Requier et al. (2019) is about 70 and 0.2 Pa s, respectively. The effective viscosity of water may be significantly higher than the molecular viscosity due to the effect of turbulence (e.g., Pope, 2000). On Enceladus, the turbulent flow may occur because of the convective heat transfer in the ocean driven by the tidal heating in the core. The effect of turbulence on the effective viscosity of the water may be further enhanced in the bottom boundary layer as a result of the hydrothermal circulation in the core (Choblet et al., 2017) and the friction at the interface. In any case, the effective viscosity is likely to vary in space and time depending on the flow conditions and the degree of turbulence. The model with a constant viscosity should therefore be viewed as a first-order approximation of the tidal flow in the ocean.

While, for the reasons outlined above, the values of the dissipation rate predicted by our simulations should be interpreted with caution, the trends inferred here are generally valid and provide context for further studies in this area. In particular, we focus on the following questions: How much is the dissipation in the ocean affected by the deformation of the core? Does the deformation of the core depend on the thickness and viscosity of the ocean? How does the velocity field in the ocean change as a function of model parameters? Is the radial component of the flow velocity significant? What are the validity limits of the LTE approach, which has been widely used to estimate heat production in subsurface oceans?

Based on the previous studies (e.g., Beuthe et al., 2016; Čadek et al., 2019b), we assume that the radius of Enceladus' core is about 190 km, and we vary the thickness of the ocean to investigate its role in different stages of Enceladus' evolution. Particular attention is paid to thin (≈ 1 km thick) ocean models that may be important for understanding the early stage of ocean formation. The results presented here may also help to clarify the role of tidal heating in the hypothetical oceans on Mimas (Tajeddine et al., 2014) and Dione (Beuthe et al., 2016; Zannoni et al., 2020) where the core may have material properties similar to those expected on Enceladus.

2. Method

We investigate the tidal deformation of an icy moon whose size and internal structure are similar to those of Enceladus. We assume that the moon consists of three layers: a solid ice shell, a liquid water ocean, and a solid core. The tidal deformation is solved simultaneously for all three layers, while the mechanical coupling between the layers is achieved by imposing continuity of traction and velocity at the boundaries. For simplicity, we assume that the boundaries are spherical, the material forming the moon is incompressible, and the tidal flow in the ocean is not affected by convective heat transport. The effect of tidal dissipation on material parameters is neglected. Under these conditions, the governing equations take the form

$$\nabla \cdot \mathbf{v} = 0, \quad (1)$$

$$\rho \left(\frac{\partial \mathbf{v}}{\partial t} + \mathbf{v} \cdot \nabla \mathbf{v} \right) = \nabla \cdot \boldsymbol{\sigma} - 2\rho \boldsymbol{\omega} \times \mathbf{v} - \rho(\nabla V_t + \nabla V_g). \quad (2)$$

Here, \mathbf{v} is the velocity, ρ is the density, t is time, $\boldsymbol{\sigma}$ is the incremental Cauchy stress tensor, $\boldsymbol{\omega}$ is the angular velocity, and V_g is the gravitational potential due to tidal deformation (for details of the calculation, see Appendix A in Čadek et al. (2021)),

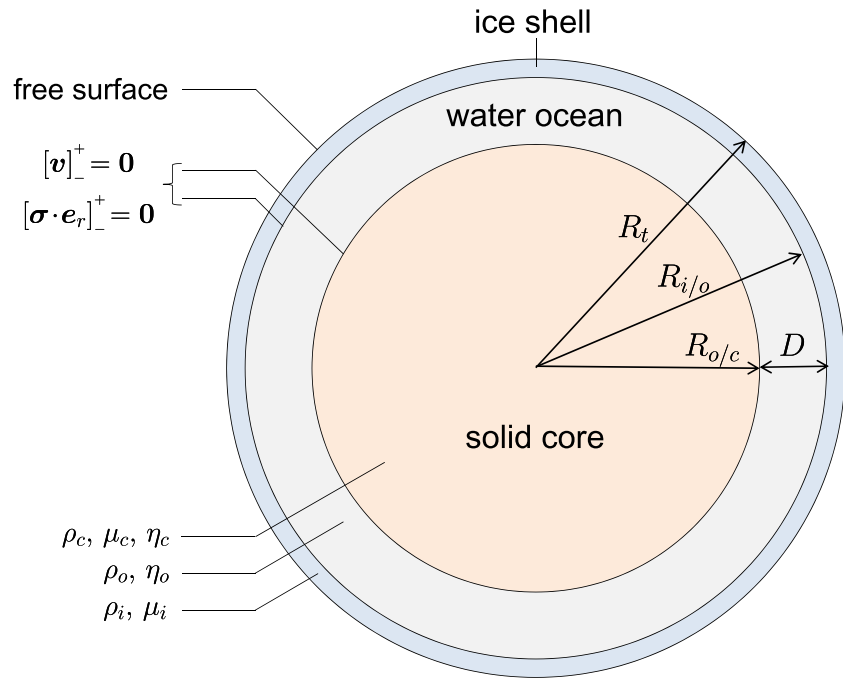


Figure 1. A sketch of the computational domain. Equations 1–5 are solved in a spherical domain made of three shells representing the solid ice crust, the liquid water ocean, and the solid silicate core. The radius of the core, $R_{o/c}$, is fixed at 194.1 km and the thickness of the ocean, D , is varied from 10 m to 50 km. We assume that the ice shell behaves as an elastic solid, while three different constitutive models of the core are considered (A–rigid, B–elastic, and C–viscoelastic). For details regarding the material parameters and the boundary conditions, see Table 1 and Equations 6 and 7, respectively.

Table 1
Parameters of the Model

Symbol	Parameter	Value	Unit
R_t	Radius of the moon	252.1	km
$R_{i/o}$	Radius of the ice/ocean interface	194.11–244.1	km
$R_{o/c}$	Radius the ocean/core interface	194.1	km
e	Eccentricity	0.0047	
ω	Angular velocity	5.31×10^{-5}	rad s ⁻¹
ρ_i	Density of the ice shell	925	kg m ⁻³
ρ_o	Density of the ocean	1,000	kg m ⁻³
ρ_c	Density of the core	2,350–2,424	kg m ⁻³
η_o	Viscosity of the ocean	10^2 – 10^6	Pa s
η_c	Viscosity of the core		
	Model A	$\rightarrow \infty$	
	Model B	$\rightarrow \infty$	
	Model C	6×10^{11}	Pa s
μ_i	Shear modulus of the ice	3.3×10^9	Pa
μ_c	Shear modulus of the core		
	Model A	$\rightarrow \infty$	
	Model B	10^9	Pa
	Model C	2×10^7	Pa

$$V_g(t, r, \vartheta, \varphi) = G \int_{\vartheta'} \int_{\varphi'} \left(\int_{R_t}^{R_t+u_t} \frac{\rho_i}{|\mathbf{r}-\mathbf{r}'|} r'^2 dr' + \int_{R_{i/o}}^{R_{i/o}+u_{i/o}} \frac{\rho_o - \rho_i}{|\mathbf{r}-\mathbf{r}'|} r'^2 dr' + \int_{R_{o/c}}^{R_{o/c}+u_{o/c}} \frac{\rho_c - \rho_o}{|\mathbf{r}-\mathbf{r}'|} r'^2 dr' \right) \sin \vartheta' d\vartheta' d\varphi' \quad (3)$$

where G is the gravitational constant, r , ϑ , and φ are the spherical coordinates, R_t , $R_{i/o}$, and $R_{o/c}$ are the radii of the density interfaces (see Figure 1) and u_t , $u_{i/o}$, and $u_{o/c}$ represent the shape changes of the boundaries. Finally, V_i is the eccentricity tidal potential valid to first order in eccentricity (Kaula, 1964),

$$V_i(t, r, \vartheta, \varphi) = r^2 \omega^2 e \left\{ \frac{3}{2} P_2^0(\cos \vartheta) \cos \omega t - \frac{1}{4} P_2^2(\cos \vartheta) [3 \cos \omega t \cos 2\varphi + 4 \sin \omega t \sin 2\varphi] \right\}, \quad (4)$$

where e is the eccentricity, and P_2^0 and P_2^2 are the associated Legendre functions. The effect of obliquity tides on the deformation of Enceladus' ocean is likely to be small (Baland et al., 2016) and is neglected.

The dimensional analysis of Equation 2 shows that the Coriolis ($2\rho\boldsymbol{\omega} \times \mathbf{v}$) and inertial ($\rho \partial \mathbf{v} / \partial t + \rho \mathbf{v} \cdot \nabla \mathbf{v}$) forces can be neglected in the ice shell and the core. In the ocean, Equation 2 can be simplified by neglecting the nonlinear term ($\rho \mathbf{v} \cdot \nabla \mathbf{v}$). The momentum equation is then linear in \mathbf{v} , and since the tidal potential is periodic, the problem can be solved in the frequency domain (Rekier et al., 2019; Rovira-Navarro et al., 2019). The simplification is usually justified by the long wavelength of the tidal forcing, or it is argued that the effect of turbulence can be included in the model by using the

effective (eddy) viscosity. In the present study, the tidal deformation is modeled in the time domain, which will allow us to assess the relative importance of the nonlinear effects and quantify the error due to the linearization of the momentum equation.

The mechanical behavior of all three layers is described by a single constitutive equation (e.g., Čadek et al., 2017),

$$\frac{1}{\mu} \frac{\partial \boldsymbol{\sigma}^d}{\partial t} + \frac{1}{\eta} \boldsymbol{\sigma}^d = \nabla \mathbf{v} + (\nabla \mathbf{v})^T, \quad (5)$$

where $\boldsymbol{\sigma}^d$ is the deviatoric part of tensor $\boldsymbol{\sigma}$. Depending on the choice of the shear modulus μ and the viscosity η , Equation 5 describes either an elastic solid ($\eta \rightarrow \infty$), a Newtonian fluid ($\mu \rightarrow \infty$) or a Maxwell viscoelastic body. Note that since the conservation laws, Equations 1 and 2, are formulated in terms of the velocity, Hooke's law, and the Maxwell constitutive equation must be expressed in terms of the strain-rate tensor.

Boundary conditions are imposed on the reference spheres of radius R_p , $R_{i/o}$, and $R_{o/c}$. Since the deformed surface of the moon is stress-free, the boundary condition at $r = R_t$ can be expressed as follows (Souček et al., 2019):

$$\boldsymbol{\sigma} \cdot \mathbf{e}_r = -\rho u_r g \mathbf{e}_r = -\rho g \mathbf{e}_r \int_0^t v_r dt', \quad (6)$$

where u_r is the radial component of the displacement, v_r is the radial component of the velocity, g is the gravitational acceleration, and \mathbf{e}_r is the radial unit vector. At the internal interfaces, the velocity and traction vectors are required to be continuous:

$$\begin{aligned} [\mathbf{v}]_{\pm}^{\pm} &= \mathbf{0}, \\ [\boldsymbol{\sigma} \cdot \mathbf{e}_r]_{\pm}^{\pm} &= \Delta \rho u_r g \mathbf{e}_r = \Delta \rho g \mathbf{e}_r \int_0^t v_r dt', \end{aligned} \quad (7)$$

where $[\cdot]_{\pm}^{\pm}$ represents the jump of the enclosed quantity across the interface and $\Delta \rho$ is the density difference ($\rho_o - \rho_i$ or $\rho_c - \rho_o$).

The total heat production of the moon is calculated using the following formula (e.g., Tobie et al., 2008):

$$H = \frac{1}{P} \int_{t_0}^{t_0+P} \int_V \frac{\boldsymbol{\sigma}^d : \boldsymbol{\sigma}^d}{2\eta} dV dt = \frac{1}{P} \int_{t_0}^{t_0+P} \int_V 2\eta \dot{\boldsymbol{\epsilon}} : \dot{\boldsymbol{\epsilon}} dV dt, \quad (8)$$

where P is the rotation period ($P = 2\pi/\omega$), t_0 is an arbitrary time, and V is the volume of the moon and $\dot{\boldsymbol{\epsilon}} = \frac{1}{2}(\nabla \mathbf{v} + (\nabla \mathbf{v})^T)$. In Section 3, the lateral variations of tidal dissipation in the ocean are characterized by the heat production integrated over the radius (Souček et al., 2019):

$$q(\vartheta, \varphi) = \frac{1}{P} \int_{t_0}^{t_0+P} \frac{1}{R_{i/o}^2} \int_{R_{o/c}}^{R_{i/o}} \frac{\boldsymbol{\sigma}^d : \boldsymbol{\sigma}^d}{2\eta} r^2 dr dt. \quad (9)$$

Data collected by the Cassini spacecraft suggest that the ocean is at a depth of about 20 km below the surface on average (Hoolst et al., 2016; Thomas et al., 2016) and that the mean ocean thickness is about 40 km (Beuthe et al., 2016; Čadek et al., 2016, 2019b). It is likely, however, that the thickness of the ocean has changed in the past and will change in the future. In order to understand the role of ocean tidal dissipation in Enceladus' evolution, we vary the thickness of the ocean from 10 m to 50 km. The lower bound of the interval corresponds to the case where the ocean is almost completely frozen but it is mechanically decoupled from the core by a thin layer of liquid water or partially molten ice. In all simulations, we assume that the radius of the core is 194.1 km (Čadek et al., 2019b) and we change the thickness of the ocean by changing the radius of the ice/ocean interface.

We assume that the ice shell behaves as an elastic solid. As shown by Souček et al. (2019) and Berne et al. (2023), the effect of viscosity on tidal deformation of Enceladus' ice shell is minor and can be neglected in the first approximation. Unfortunately, there are presently no observations to constrain the material parameters of Enceladus' core. In most of the previous studies on the ocean tides, the core was assumed to be rigid and its effect on the flow in the ocean was neglected. However, if the core has never been exposed to high temperatures and pressures, the core material may still be in an unconsolidated, fragmented state and may effectively behave as a

low rigidity, low viscosity viscoelastic body (Choblet et al., 2017; Roberts, 2015; Rovira-Navarro et al., 2022; Travis & Schubert, 2015). If this is the case, the tidal deformation of the core may affect the flow in the ocean in a similar way as the tidal deformation of the ice shell. Here we consider three models of the core: A—the rigid core, B—the elastic core with $\mu_c = 10^9$ Pa (cf. Roberts, 2015), and C—the viscoelastic core with $\mu_c = 2 \times 10^7$ Pa and $\eta_c = 6 \times 10^{11}$ Pa s. The parameters of model C are chosen so that the total heat production of the core is roughly 25 GW (cf. Figure 1a in Choblet et al. (2017)). The parameters of models A–C are summarized in Table 1.

Equations 1–7 are solved in the time domain using a pseudo-spectral method similar to that used by Kverka and Čadek (2022). The unknown functions \mathbf{v} and $\boldsymbol{\sigma}$ are represented in terms of the generalized spherical harmonic expansions (e.g., Golle et al., 2012), truncated at degree ℓ_{\max} . The cut-off degree ℓ_{\max} is chosen so that $V(\ell_{\max})V(2) < 10^{-4}$, where $V(\ell)$ denotes the L_2 norm of the velocity field at degree ℓ , and ranges from 10 to 220 depending on the thickness and viscosity of the ocean. The coefficients in the harmonic series are discretized in the radial direction on an uneven grid consisting of 800 Chebyshev nodes (for an example of the radial resolution, see Figure S1 in Supporting Information S1). The radial resolution varies from 1 m in the ocean boundary layers to 1.5 km in the ice shell and the core. The time derivatives in Equations 2 and 5 are discretized using the implicit Euler method, while the explicit second-order Adams-Bashforth method is applied to the Coriolis and non-linear terms. Each simulation is started from the initial condition $\mathbf{v} = \mathbf{0}$, and the equations are integrated in time until a periodic solution is reached (cf. Běhouňková et al., 2010; Tobie et al., 2008). At each time step, the accuracy of the method is assessed by evaluating the energy balance (Patočka et al., 2017). The numerical method was coded in Fortran 90 and tested against the results by Beuthe (2016) and Requier et al. (2019), see Section 5 and Figure S2 in Supporting Information S1.

3. Tidal Dissipation in the Ocean and the Core

Figure 2 shows the tidal dissipation in the ocean (Figures 2a–2c) and the core (Figure 2d) as a function of ocean thickness for different values of ocean viscosity. Comparison of Figures 2a–2c reveals two general trends: (a) The maximum heat production in the ocean is independent of the viscosity of the ocean but depends on the material properties of the core ($H = 4$ GW for model A but 20 GW for model C). The value of D at which the maximum is reached is less than 2 km and decreases with decreasing viscosity. (b) When the ocean thickness is larger than 5 km, the curves are similar in shape to those obtained by Requier et al. (2019) and Rovira-Navarro et al. (2019). The curves are characterized by several resonance peaks whose amplitudes increase with decreasing viscosity. The dissipation in the ocean is less than 0.1 GW and thus insufficient to explain the heat output (>10 GW) of present-day Enceladus ($D = 38$ km).

The maximum heat production obtained for model A (stiff core) is twice as high as for model B (elastic core). This somewhat counterintuitive result is due to the fact that, in the elastic case, the upper and lower boundaries move in phase, and consequently, the radial deformation of the fluid layer is smaller than in the case of the rigid core. The parameters of model C are chosen such that the deformation of the ocean/core boundary is significantly larger than that of the elastic shell. The Deborah number of the core (τ_M/P where $\tau_M = \eta_c/\mu_c$ is the Maxwell time and P is the rotation period) is about 0.25, implying that the tidal response of the core is dominated by viscous flow. This, together with the fact that the response of the core to the tidal force is delayed, results in an enhancement of the heat production in the ocean (Figure 2c). The maximum heat production is about 20 GW and is attained for a slightly larger value of D than in models A and B (70 m–2.5 km, depending on η_o). This suggests that tidal dissipation in a thin ocean may be sufficiently high to prevent the ocean from freezing.

The thickness of the ocean influences not only the dissipation in the ocean itself but also in the viscoelastic core (Figure 2d). When the thickness of the ocean drops below a critical value, D_{crit} , the heat production in the core starts to decrease rapidly. The thickness of the ocean at which the drop occurs roughly corresponds to the thickness at which the dissipation in the ocean reaches a maximum value (cf. Figures 2c and 2d). Note that the heat production in the core for $D > D_{crit}$ is the same as the maximum heat production in the ocean, suggesting that at $D \approx D_{crit}$ the role of the core as the main producer of heat is taken over by the ocean. When the ocean thickness is further decreased, the heat production in the ocean goes to zero, and the total tidal heat production of the moon approaches a value of 0.25 GW, corresponding to dissipation in a viscoelastic core surrounded by a shell of elastic ice.

As already mentioned in Section 2, our approach is different from the one used by Requier et al. (2019) in that the deformation equations are solved simultaneously in the whole domain (including the solid parts) while Requier

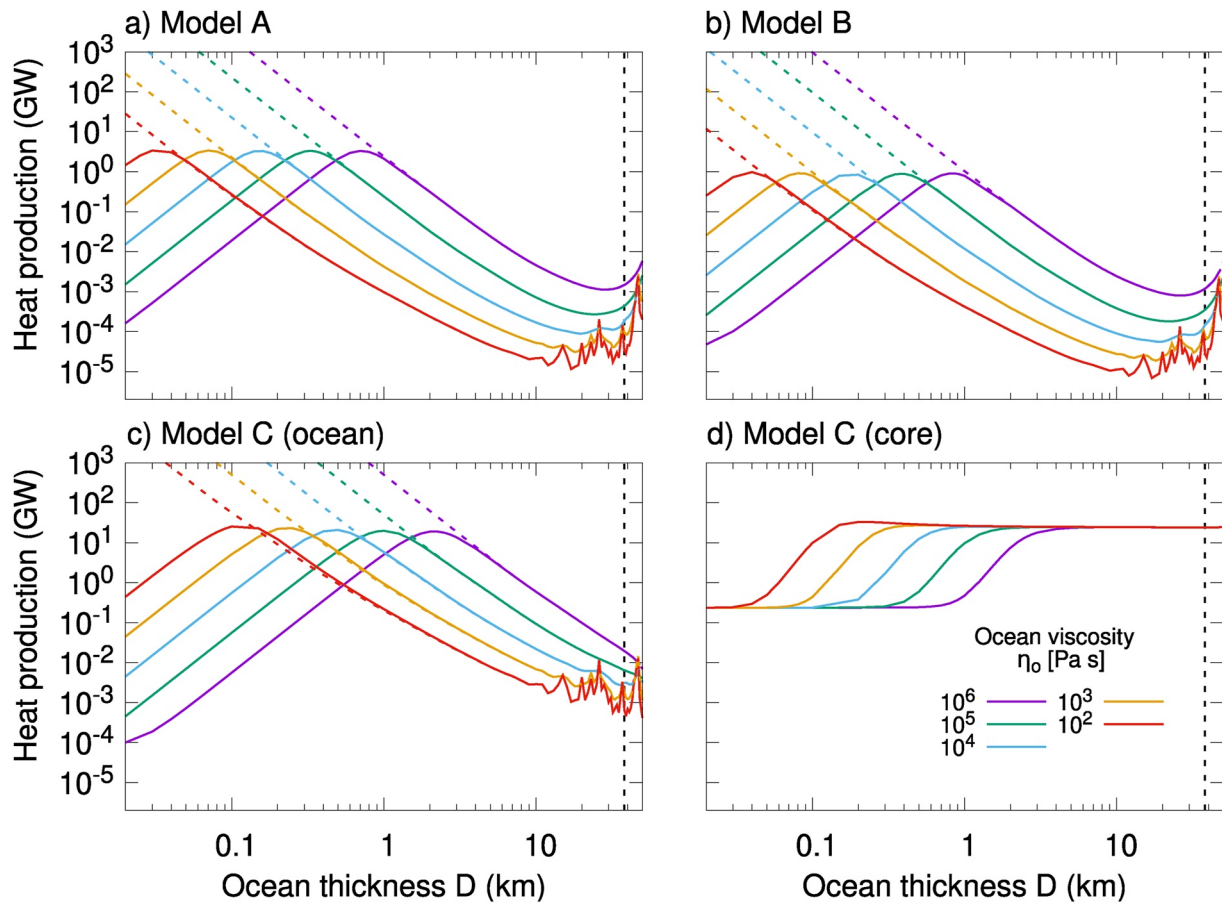


Figure 2. Heat production in (a–c) Enceladus' ocean and (d) core as a function of ocean thickness evaluated for different values of viscosity η_o . Heat production in the core is shown only for model C since the core in models A and B is treated as non-dissipative ($\eta_c \rightarrow \infty$). The solid lines represent models where the deformation equations are solved in the whole domain (including the solid parts, see Section 2), while the colored dashed lines correspond to models where the flow is solved only in the ocean and the deformation of the ice shell the core is implemented through boundary conditions (Rekier et al., 2019). The vertical black dashed lines indicate the current thickness of Enceladus' ocean.

et al. (2019) first calculate the deformation of the ice shell and the core and then use it as a boundary condition to compute the flow in the ocean. Comparison of the solid and dashed lines in Figures 2a–2c shows that the two approaches give the same heating rates for $D > D_{crit}$, implying that the flow in the ocean has little impact on the deformation of the ice shell and the core if the ocean thickness is larger than about 2 km. However, the approach where the deformation of the solid parts is not self-consistently included grossly overestimates the tidal dissipation in the ocean for $D < D_{crit}$. It is likely that Rekier et al. (2019) anticipated this behavior and therefore only considered models where $R_{olc}/R_{ilo} < 0.98$ (corresponding to $D \approx 4$ km). The large discrepancy between the two solutions suggests that the assumption that the deformation of the ice shell and the core is independent of the tidal flow in the ocean is not valid for $D < D_{crit}$. This implies that the mechanical coupling between the ocean and the solid parts of the moon must be considered when evaluating dissipation in a thin ocean.

The flow induced by eccentricity tides in Enceladus' ocean yields a wide variety of heating patterns depending on the thickness of the ocean and its viscosity (Figures 3 and 4). For some combinations of parameters η_o and D , the heat flux distribution is similar to those obtained using the shallow water approximation (see Figure 4 in Tyler et al. (2015) or Figure 7 in Matsuyama et al. (2018)). In most cases, however, the heat flux distribution is rather complex, indicating that dissipation in the ocean is strongly influenced by three-dimensional flow effects. The heat flux distribution obtained for $D = 47$ km and $\eta_o \leq 10^4$ Pa s, characterized by a system of concentric circular fringes, is compatible with the presence of inertial waves discussed by Rovira-Navarro et al. (2019) and Rekier et al. (2019).

The spatial distribution of the tidal heat produced in the core is independent of the viscosity and thickness of the ocean and only differs by magnitude. Similar to the results of Roberts (2015, Figure 3b) and Choblet et al. (2017,

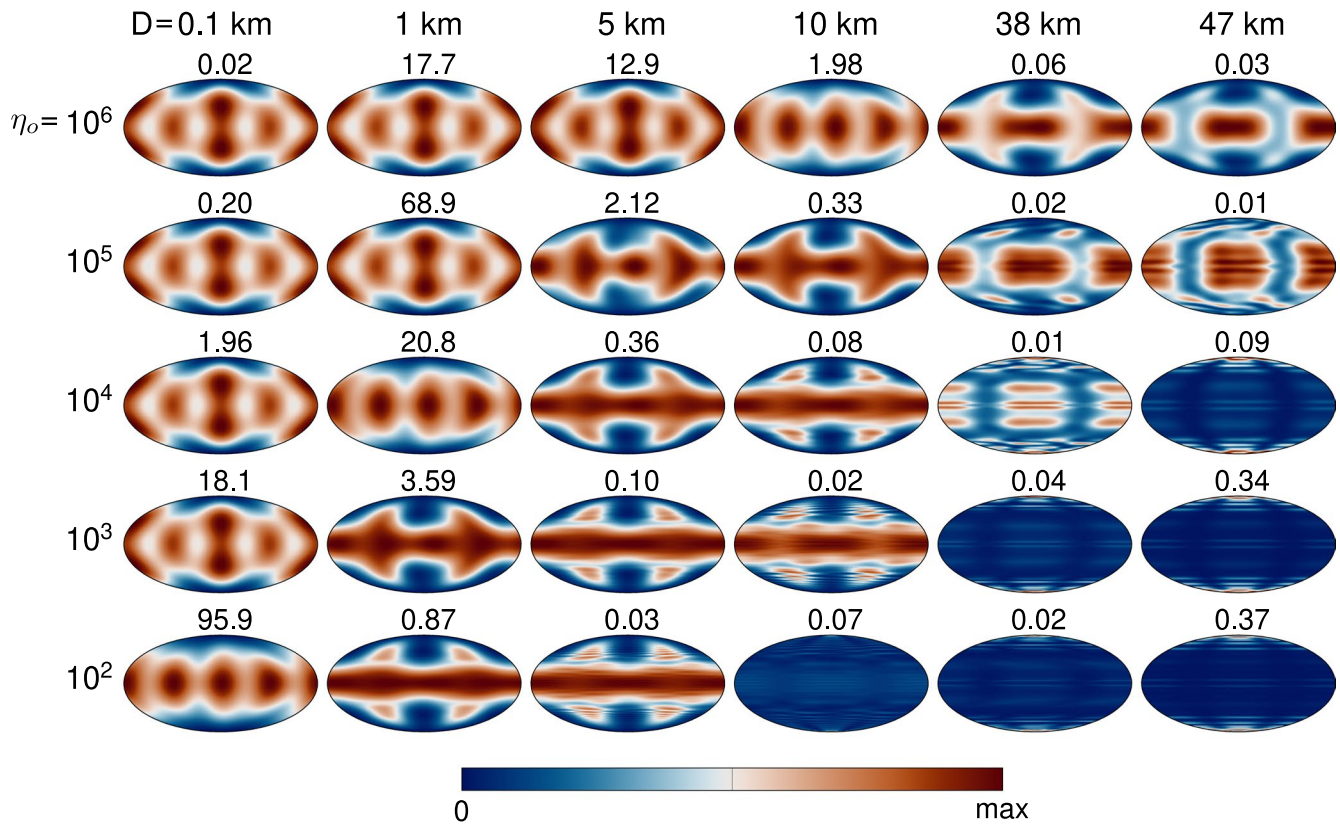


Figure 3. Surface distribution of ocean tidal heating averaged over the tidal cycle, Equation 9, for different thicknesses (columns) and viscosities (rows) of the ocean. All heat flux maps are computed for model C and shown in the Mollweide projection with the sub-Saturnian point at the center. For the sake of comparison of the heating patterns, each map is scaled to its own maximum (indicated above the map in mW/m^2).

Figure 1c), the maximum heat flux is concentrated over the polar regions, reaching the value of about 70 mW/m^2 for $D > D_{crit}$ and 0.66 mW/m^2 when $D \rightarrow 0$ (see also Figure S3 in Supporting Information S1).

4. Velocity Field in the Ocean

A number of studies of ocean tides have been based on the assumption that the horizontal scale of flow is much larger than the depth of the ocean. Under this assumption, the trajectories of water parcels are nearly horizontal, the radial velocity is small compared to the horizontal velocity and the Navier-Stokes equations can be reduced to a two-dimensional form, called the Laplace tidal (or shallow water) equations, in which the horizontal velocity is a function of only ϑ and φ . The equations do not contain the radial component of velocity and the effect of radial flow on the viscous, inertial, and Coriolis force is neglected (Tyler, 2008). In this section, we will address the limitations of this approach and demonstrate the complex structure of the tidal flow in Enceladus' ocean. We will follow up on the studies by Rovira-Navarro et al. (2019) and Requier et al. (2019) that have investigated the tidal response of a subsurface ocean by solving the three-dimensional Navier-Stokes equations. However, unlike these studies, we will present the flow field distribution not in the frequency domain but in the time domain, and we will examine the importance of the non-linear term in the momentum equation, which has been neglected in previous research.

In Figure 5, we show the velocity field at time $t = 0$ for models with $\eta_o = 100 \text{ Pa s}$ and D ranging from 0.1 to 47 km. Note that for clarity, the thickness of the ocean in the visualization is fixed at $D = 0.25R_{olc} \approx 50 \text{ km}$. Inspection of the figure shows that the assumption of shallow water is well satisfied for $D \lesssim 1 \text{ km}$ but breaks down when $D \gtrsim 5 \text{ km}$. When $D = 38 \text{ km}$ (corresponding to the average ocean thickness at present), the radial and tangential components are the same size, and the horizontal scale of the flow is comparable with the thickness of the ocean, suggesting that the shallow water approach is not suitable for modeling Enceladus' ocean tides.

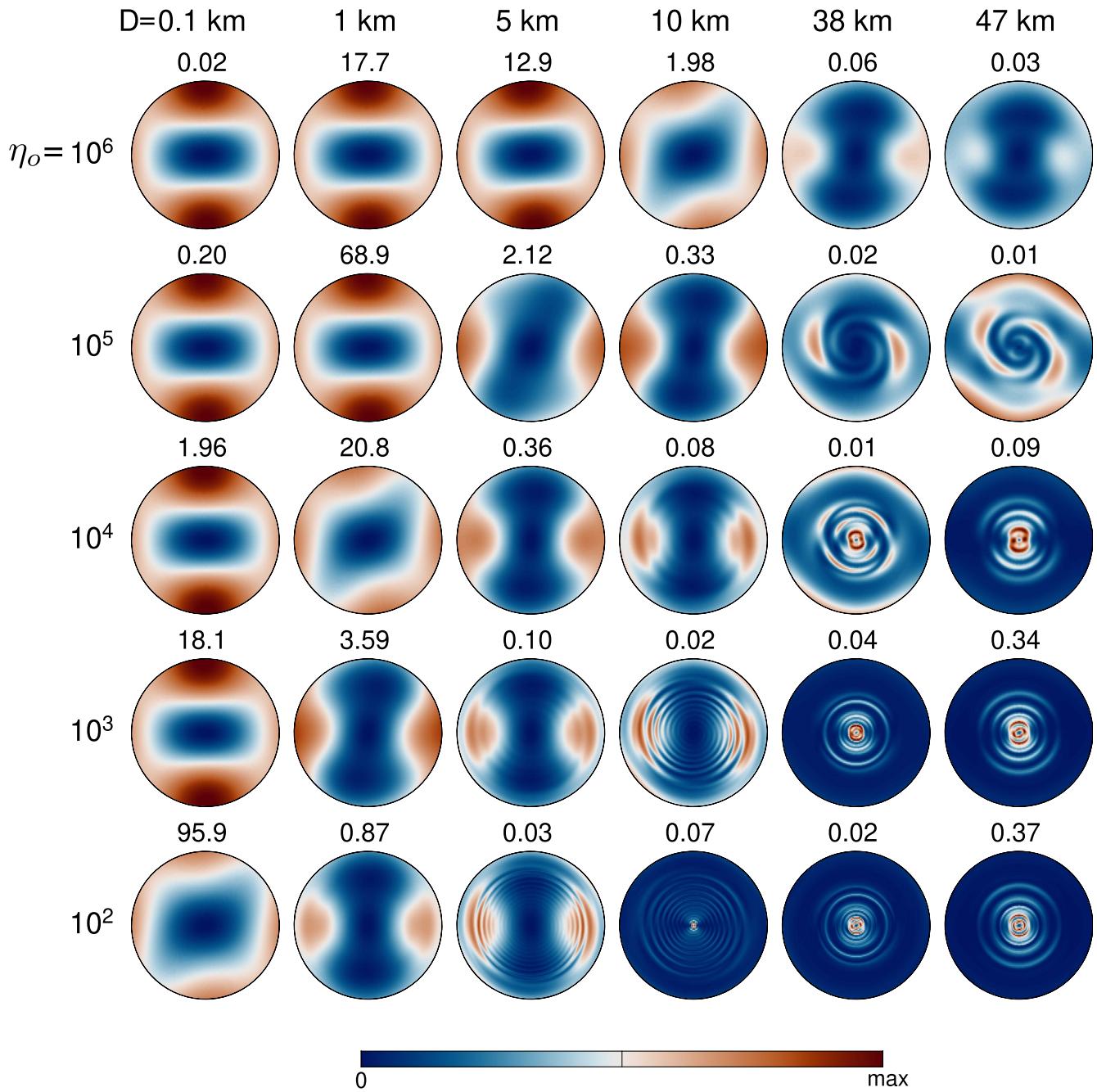


Figure 4. As in Figure 3 but in North pole stereographic projection.

Figure 6 shows the same flow models as Figure 5 but in North pole stereographic projection. The velocity fields represented by surface streamlines are shown at a depth of $D/10$ below the ice/ocean boundary. A long-wavelength flow pattern typical of shallow water models is found only for $D \leq 5$ km. For larger values of D , the velocity field is dominated by small-scale concentric flow loops rotating in the azimuthal direction that cannot be obtained using the standard shallow water approach.

Previous studies of tidal flow in subsurface oceans have assumed that the non-linear term in the momentum equation ($\rho \mathbf{v} \cdot \nabla \mathbf{v}$) can be neglected or its effect can be simulated by a global increase in viscosity (i.e., by using the eddy viscosity instead of the molecular viscosity). The problem of tidal flow is then linear in \mathbf{v} , and its solution shows a marked resonant behavior characterized by a significant increase in the kinetic energy of the flow (e.g.,

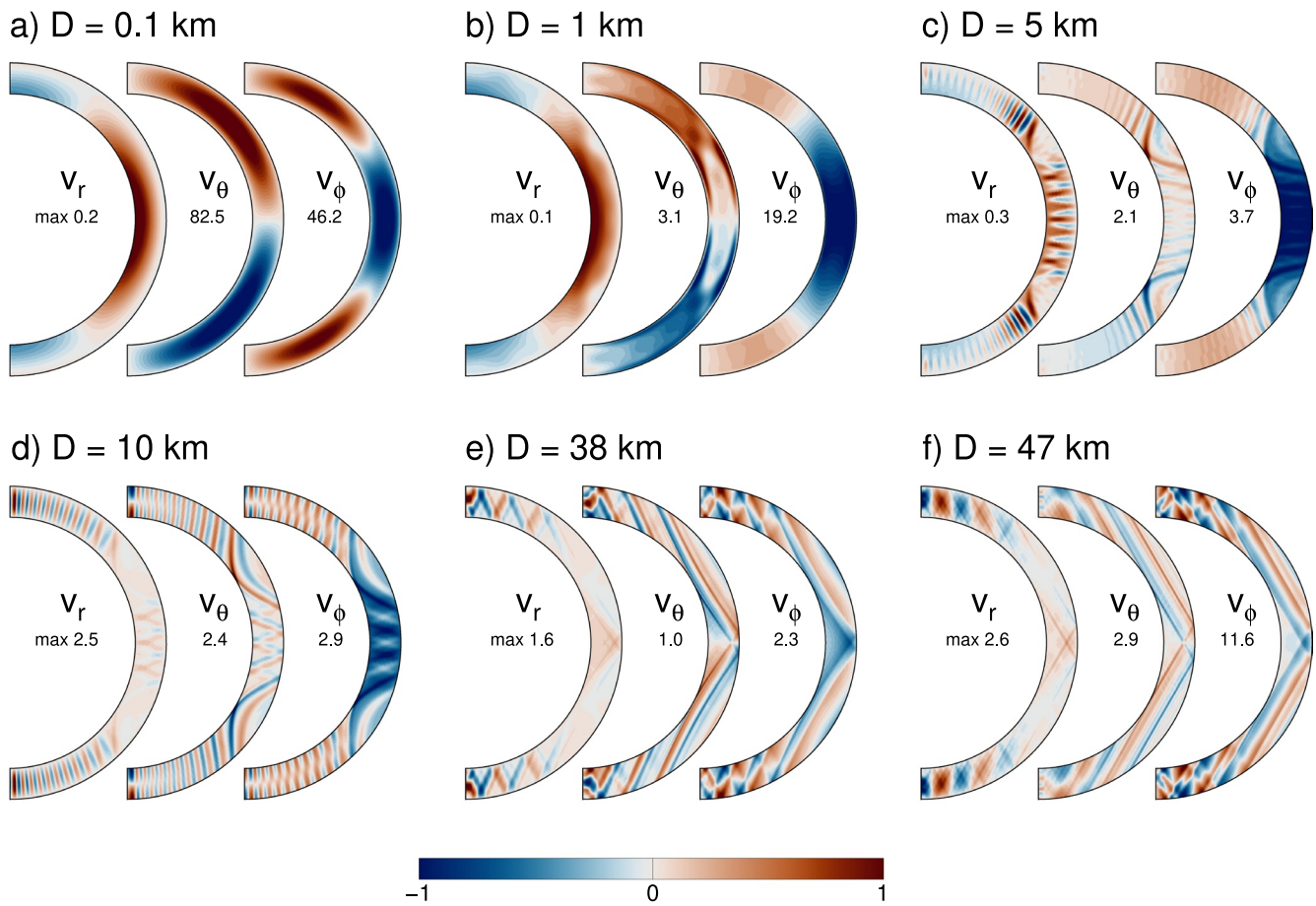


Figure 5. Velocity fields (components r , θ , and ϕ) at time $t = 0$ obtained for $\eta_o = 100$ Pa s and D ranging from 0.1 to 47 km. The fields are normalized to 1 and plotted on a meridional cross-section at longitude $\phi = 0$. The maximum values in mm/s are given on the left-hand side of each cross-section. While the ratio D/R_{olc} varies from 5.2×10^{-4} in panel (a) to 0.24 in panel (f), the thickness of the ocean in the visualization is fixed at $D/R_{olc} = 0.25$ for clarity.

Tyler, 2008). The question arises as to how much this behavior would be affected by the non-linear term and, in general, what role turbulence plays in tidal dissipation. One way to assess whether the flow is turbulent or not is to evaluate the Reynolds number, $Re = \rho_o |v| D / \eta_o$, where $|v|$ is the L_2 norm of the velocity field. The Reynolds number is a dimensionless quantity that is used to predict the transition from laminar to turbulent flow. Turbulent flow occurs when $Re > Re_c$ where Re_c is the critical Reynolds number ($Re_c = 10^3 - 10^4$, depending on the geometry of the system). As shown in Figure 7a, all models presented in this study ($\eta_o \geq 100$ Pa s, $D \leq 50$ km) are characterized by low Reynolds numbers ($Re \lesssim 1,000$), suggesting the dominant role of laminar flow. This conclusion is supported by a direct comparison of the terms in the NSE, which is obtained by substituting σ from Equation 5 into Equation 2 and setting $\mu^{-1} = 0$,

$$\rho \left(\frac{\partial \mathbf{v}}{\partial t} + \mathbf{v} \cdot \nabla \mathbf{v} \right) = -\nabla p + \eta \nabla \cdot \nabla \mathbf{v} - 2\rho \boldsymbol{\omega} \times \mathbf{v} - \rho (\nabla V_t + \nabla V_g), \quad (10)$$

where p is the pressure. Figure 7b shows that the non-linear term ($\rho \mathbf{v} \cdot \nabla \mathbf{v}$), which is responsible for turbulence, is small compared to other terms in Equation 10. Extrapolation of the results shown in Figure 7a indicates that the transition from laminar to turbulent flow occurs when the viscosity η_o drops to about 10 Pa s, presumably leading to an increase of the Reynolds number to $10^3 - 10^4$. We are currently unable to perform time domain simulations for $\eta_o \ll 100$ Pa s because they place extreme demands on the numerical resolution required to represent the velocity fields. The problem of whether the turbulent flow can influence the resonant states predicted by the linearized model thus remains unresolved and will require further improvements of the numerical method.

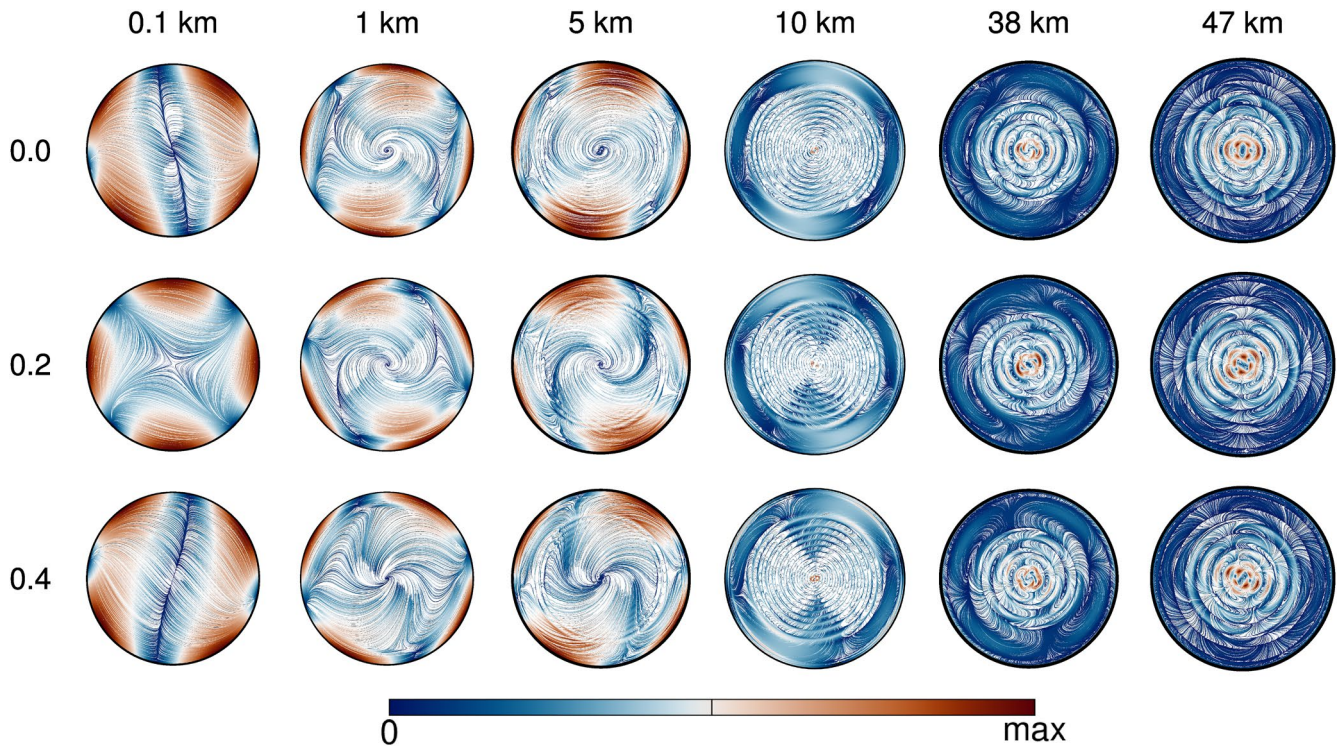


Figure 6. Horizontal component of the flow velocity, $\mathbf{v} - (\mathbf{v} \cdot \mathbf{e}_r)\mathbf{e}_r$, at a depth of $D/10$ below the ocean surface computed in different orbital phases ($t = 0, 0.2,$ and $0.4 P$) for the same models as in Figure 5. The horizontal velocity is represented by streamlines with colors representing the flow speed. All maps are shown in the North pole stereographic projection.

5. Comparison With the LTE Approach

In this section, we compare our approach with that of Beuthe (2016). To couple the flow in the ocean with the deformation of the ice shell, Beuthe (2016) formulated the LTE as follows:

$$\frac{\partial \mathbf{u}}{\partial t} = -\frac{1}{\rho_o} \nabla_s p - 2\boldsymbol{\omega} \times \mathbf{u} + \mathbf{F}(\mathbf{u}), \quad (11)$$

$$\frac{\partial h}{\partial t} + D\nabla_s \cdot \mathbf{u} = 0, \quad (12)$$

$$p = \Delta \rho g h - \rho_o (V_i + V_g) - \sigma_{rr}. \quad (13)$$

Here, $\mathbf{u} = \mathbf{u}(\vartheta, \varphi)$ is the depth-averaged velocity, ∇_s is the surface gradient, h is the radial displacement at the boundary between the ice shell and the ocean, σ_{rr} is the radial component of the traction vector at the base of the ice shell, and $\mathbf{F}(\mathbf{u})$ represents the dissipative stress

$$\mathbf{F}(\mathbf{u}) = \frac{\eta_o}{\rho_o} \Delta_s \mathbf{u} - \alpha \mathbf{u}, \quad (14)$$

where α is the linear drag coefficient and Δ_s is the horizontal Laplace operator. Unlike the previous studies (e.g., Chen et al., 2014; Matsuyama, 2014; Tyler, 2014), the approach by Beuthe (2016) includes the stabilizing effect of the overlying shell, which damps the ocean tides and reduces the tidal heating in the ocean (see also Matsuyama et al. (2018)). In the following, Equations 11–14 are referred to as the modified LTE.

The modified LTE approach differs from our approach, Equations 1–7, in two ways. First, as already mentioned above, the modified LTE approach does not include the radial component of velocity and assumes that the horizontal velocity is a function of only ϑ and φ (i.e., $\partial \mathbf{u} / \partial r = 0$). Second, the modified LTE approach guarantees that the radial components of the displacement and traction do not change across the ice/ocean boundary (Equation 13), but, for understandable reasons, it imposes no restriction on the horizontal components (in other

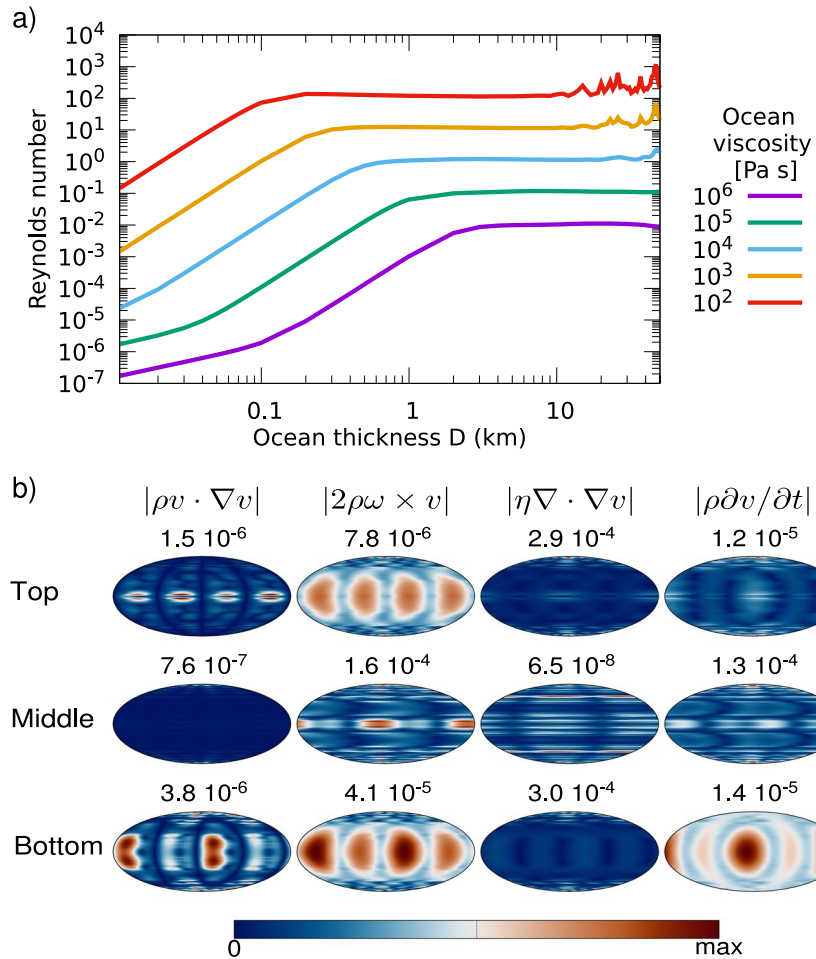


Figure 7. (a) The Reynolds number as a function of ocean thickness evaluated for different values of viscosity η_o . (b) Comparison of the terms in the Navier-Stokes Equation 10 near the top and bottom boundaries and in the middle of the ocean for the model with $D = 38$ km and $\eta_o = 100$ Pa s. The numbers above the plots indicate the maximum values in N/m^3 .

words, the boundary is free-slip). In contrast, in our approach, we assume that the boundary is no-slip and both radial and horizontal components of the displacement and traction are continuous (Equation 7).

To facilitate the comparison of the methods, we replace the no-slip boundary condition in our model with the free-slip one and omit the last term in Equation 14 because the drag coefficient α is not included in our 3D model. The modified LTE method has been coded in Fortran 90 and tested against the results of Beuthe (2016). Unlike the original method (Beuthe, 2016) where the layer overlying the ocean is treated as a thin shell, the stress and displacement in the ice are obtained by solving the standard equations for thick shells (cf. Matsuyama et al., 2018). The total heat production of the 3D model can be calculated from Equation 8. For the sake of comparison with the modified LTE approach, we replace the velocity \mathbf{v} in Equation 8 by the depth-averaged velocity, $\bar{\mathbf{v}}$:

$$H = \frac{2\eta D}{P} \int_{t_0}^{t_0+P} \int_S \dot{\bar{\mathbf{e}}} : \dot{\bar{\mathbf{e}}} dS dt, \quad (15)$$

where S is the surface of the sphere of radius R_{io} and $\dot{\bar{\mathbf{e}}} = \frac{1}{2} (\nabla_s \bar{\mathbf{v}} + (\nabla_s \bar{\mathbf{v}})^T)$. Note that $\bar{\mathbf{v}} = \mathbf{u}$ in the case of the modified LTE method.

The heat production obtained for the two methods is compared in Figure 8a. The calculations are performed only for model A (i.e., the model with a rigid core). Inspection of the figure shows that the level of agreement between the methods depends not only on the thickness of the ocean but also on the viscosity of water and on how the dissipation rate of the 3D model is calculated. Our results indicate that for the low values of the viscosity

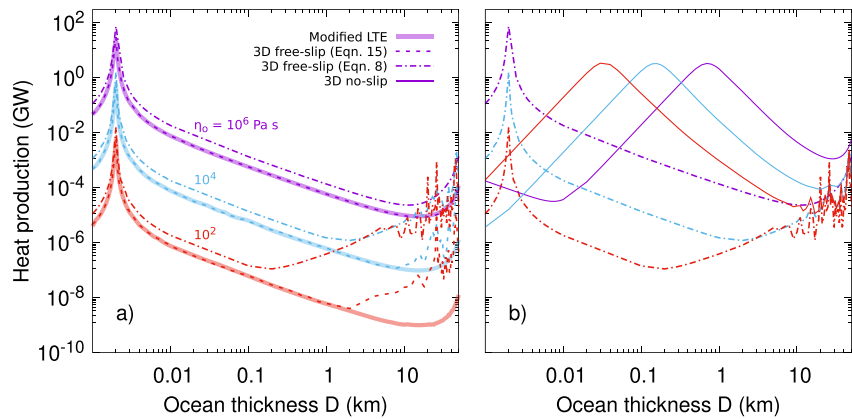


Figure 8. (a) Dissipation as a function of the ocean thickness computed using the modified Laplace tidal equations approach by Beuthe (2016, thick solid lines) and the 3D approach (this study) in which the no-slip boundary conditions were replaced by the free-slip ones (dashed and dash-dotted lines). Dissipation in the 3D models is obtained using either Equation 8 or Equation 15. The violet, blue, and red colors represent different values of viscosity η_0 . (b) Comparison of 3D free-slip (dash-dotted lines) and 3D no-slip solutions (thin solid lines) obtained for model A (see Table 1). Colors are the same as in panel (a). All the calculations are performed for model A.

($\eta \lesssim 100$ Pa s), the modified LTE method is only applicable to models with very thin ocean ($D \lesssim 2$ km). On the other hand, when the viscosity is high ($\eta = 10^6$ Pa s), the modified LTE method and the 3D method show good agreement over the whole range of ocean thickness.

The agreement between the LTE and 3D solutions is generally better when the heat production of the 3D model is calculated from Equation 15. When depth variations in velocity are included, that is, when H is calculated from Equation 8, the heat production increases and the difference between the modified LTE solution and 3D solution is significant even for ocean thicknesses as small as 10 m. The difference is more pronounced for models with a low viscosity ocean, ranging from a factor of 2 at $D \leq 100$ m to a factor of 10^5 at $D = 50$ km for $\eta = 100$ Pa s. This indicates that depth variations in velocity play an important role in calculating the tidal heat production even when $DR_{ilo} \ll 1$ (see Figure S4 in Supporting Information S1). These variations are inherently absent in the modified LTE solution, casting doubt on the applicability of the LTE method for determining the dissipation rate in the ocean. It is also worth noting that the dissipation curves computed for 3D models where the internal interfaces are treated as free-slip boundaries are significantly different from those computed for 3D models with no-slip boundaries. To allow for a better comparison between the free-slip and no-slip solutions, the two sets of curves are shown together in Figure 8b.

No-slip is usually considered to be the appropriate boundary condition for a viscous fluid in contact with a solid impermeable surface. More generally, the boundary condition can be expressed as a weighted combination of no-slip and free-slip boundary conditions:

$$v_r = 0, \quad (16)$$

$$(\boldsymbol{\sigma} \cdot \mathbf{e}_r)_r = -\alpha \mathbf{v}, \quad (17)$$

where the subscripts r and τ denote the radial and tangential components, respectively, and α is the drag coefficient, which may depend on the velocity. The boundary condition 17 reduces to no-slip boundary condition for $\alpha \rightarrow \infty$ and to the free-slip boundary condition for $\alpha = 0$. No-slip and free-slip can therefore be considered as extreme cases.

Unlike the free-slip model, the no-slip model is characterized by the presence of velocity boundary layers, the thin layers of fluid in the vicinity of the boundaries where the flow velocity monotonically increases with the distance from the boundary (Figure 9a). Although the velocity far from the boundary may not be affected by the type of the boundary condition (i.e., by the presence or absence of the boundary layer), the dissipation, which depends on the gradient of velocity, is usually higher for no-slip models compared to free-slip models. Nearly all of the tidal dissipation in the no-slip models is concentrated in the boundary layers (Figure 9b) and even though the thickness

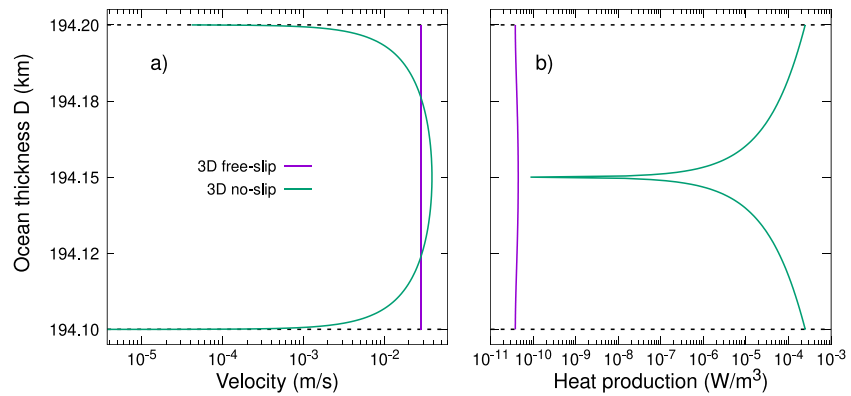


Figure 9. Radial variation of the (a) mean flow velocity and (b) heat production in the ocean for $D = 100$ m, $\eta_o = 100$ Pa s, and $t = 0$. The violet and green lines represent the 3D models with the free-slip and no-slip conditions, respectively. The mean velocity is calculated as $\sqrt{\int_S |\mathbf{v}(r, \theta, \varphi)|^2 dS}$ while the mean heat production is given by $2\eta_o S^{-1} \int_S \dot{\epsilon} : \dot{\epsilon} dS$.

of the boundary layers is small, the total heat production can be up to six orders of magnitude higher than in the corresponding free-slip models.

6. Conclusion

In this study, we have presented a novel approach to modeling the tidal response of icy moons with subsurface oceans. The problem of tidal deformation is solved in the time domain and the flow in the ocean is calculated simultaneously with the deformation of the core and the ice shell. The main advantage of this approach is that it makes it possible, at least in principle, to investigate the non-linear effects associated with turbulent flow. However, this advantage is also its biggest limitation: Since the time required to reach a stable periodic or quasi-periodic solution is rather long (~ 100 – $1,000 P$), the calculations are time-consuming and at present are only feasible for viscosities that are several orders of magnitude higher than the molecular viscosity of water.

The method developed here is used to study the tidal flow in the ocean of Enceladus. In particular, we focus on the role of a highly deformable and dissipative core in ocean dynamics and investigate the mechanical coupling between the core and the ocean. We show that the amount of tidal heat generated in the core and the ocean strongly depends on the thickness of the ocean layer. If the ocean thickness is significantly greater than 1 km, heat production is dominated by tidal dissipation in the core and the amount of heat produced in the ocean is negligible. In this case, tidal deformation of the core and crust is unaffected by tidal currents in the ocean, implying that tidal flow in the ocean can be investigated using the approach by Rekier et al. (2019) where the deformations of the crust and core are computed beforehand and imposed as boundary conditions. In contrast, when the ocean thickness is less than about 1 km, tidal heating in the core diminishes and dissipation in the ocean increases, leaving the total heat production unchanged. The maximum heat production in the ocean depends only on the material properties of the core and may exceed 20 GW if the core is highly deformable.

We demonstrate that the flow pattern and the distribution of tidal dissipation strongly depend on the thickness of the ocean. The radial component of the velocity is found to be negligible only if the ocean thickness is less than about 5 km, implying that the shallow water approximation (Tyler, 2009, 2020) is not applicable to present-day Enceladus. The amount of small-scale content in the velocity field increases with decreasing viscosity and increasing ocean thickness, leading to complex patterns of heat flux at the surface of the ocean.

Comparison of our results with those obtained using the LTE approach by Beuthe (2016) suggests that the shallow water equations corrected for the dampening effect of the ice shell give a reasonable estimate of the horizontal flow velocity but they fail to predict the correct values of the dissipation rate. The reason for this is that the solution of these equations cannot, in principle, provide information about the radial changes of the velocity vector. We show that these changes play an important role in calculating the dissipation and may be significant even in the case of a thin ocean.

Extrapolation of our results to realistic (low viscosity) conditions indicates that the heat production in Enceladus' present-day ocean is likely to be less than 0.1 GW, corresponding to 0.25% of Enceladus' total heat loss. This

suggests that the tidal dissipation in the ocean plays a minor role in Enceladus' heat budget, which is in agreement with most of the recent studies, except the one by Tyler (2020). It is unclear, however, whether such an extrapolation is justified because the models of ocean tides presented here are characterized by laminar flow (Reynolds number $\lesssim 10^3$) while the flow in the real ocean is likely to be turbulent. Based on our results, we estimate that the onset of turbulence occurs when the model viscosity drops below 10 Pa s, that is, at a value that is still rather high compared to the molecular viscosity of water. The reader should be aware that the results presented here may be affected by the fact that our model does not include the effect of ocean thickness variations and stratification, which can significantly enhance the dissipative processes in the ocean.

The question of to what extent the non-linear effects and possible resonant interactions can influence tidal dissipation in the ocean has not been addressed in previous studies. Some of these studies (e.g., Matsuyama, 2014; Requier et al., 2019; Rovira-Navarro et al., 2019; Tyler, 2014) have demonstrated that the solution of the linearized NSE exhibits strong resonance peaks occurring when the system is able to store the tidal energy and transfer it into kinetic energy. However, the increase in the kinetic energy would likely result in the onset of turbulence, violating the assumption of linearity, enhancing the damping properties of the system, and possibly reducing the amplitude of flow oscillations. Understanding these effects will require a thorough analysis of tidal flow at small spatial scales. This goal can hardly be achieved without the development of new numerical tools that will make it possible to perform high resolution simulations in the time domain. We believe this study is a first step toward this goal.

Data Availability Statement

The data regarding the figures and the code that computes the three-dimensional tidal dissipation are available in the Zenodo repository (Aygün & Čadek, 2023).

Acknowledgments

We thank an anonymous reviewer for helpful comments that improved the manuscript, Mikael Beuthe for his help in comparing our results with the solution of the Laplace tidal equations, and Jérémy Requier for providing us with the results of his 3D simulations. B.A. acknowledges the support from the Charles University Project SVV 260709.

References

- Aygün, B., & Čadek, O. (2023). Data and software for the article "Impact of the core deformation on the tidal heating and flow in Enceladus' subsurface ocean". Zenodo. <https://doi.org/10.5281/zenodo.10057002>
- Baland, R.-M., Yseboodt, M., & Hoolst, T. V. (2016). The obliquity of Enceladus. *Icarus*, 268, 12–31. <https://doi.org/10.1016/j.icarus.2015.11.039>
- Běhouňková, M., Souček, O., Hron, J., & Čadek, O. (2017). Plume activity and tidal deformation on Enceladus influenced by faults and variable ice shell thickness. *Astrobiology*, 17(9), 941–954. <https://doi.org/10.1089/ast.2016.1629>
- Běhouňková, M., Tobie, G., Choblet, G., & Čadek, O. (2010). Coupling mantle convection and tidal dissipation: Applications to Enceladus and Earth-like planets. *Journal of Geophysical Research*, 115(E9), E09011. <https://doi.org/10.1029/2009JE003564>
- Berne, A., Simons, M., Keane, J. T., & Park, R. S. (2023). Inferring the mean thickness of the outer ice shell of Enceladus from diurnal crustal deformation. *Journal of Geophysical Research: Planets*, 128(6), e2022JE007712. <https://doi.org/10.1029/2022JE007712>
- Beuthe, M. (2016). Crustal control of dissipative ocean tides in Enceladus and other icy moons. *Icarus*, 280, 278–299. <https://doi.org/10.1016/j.icarus.2016.08.009>
- Beuthe, M., Rivoldini, A., & Trinh, A. (2016). Enceladus's and Dione's floating ice shells supported by minimum stress isostasy. *Geophysical Research Letters*, 43(19), 10088–10096. <https://doi.org/10.1002/2016GL070650>
- Čadek, O., Běhouňková, M., Tobie, G., & Choblet, G. (2017). Viscoelastic relaxation of Enceladus's ice shell. *Icarus*, 291, 31–35. <https://doi.org/10.1016/j.icarus.2017.03.011>
- Čadek, O., Kalousová, K., Kverka, J., & Sotin, C. (2021). The density structure of Titan's outer ice shell. *Icarus*, 364, 114466. <https://doi.org/10.1016/j.icarus.2021.114466>
- Čadek, O., Souček, O., & Běhouňková, M. (2019a). Is Airy isostasy applicable to icy moons? *Geophysical Research Letters*, 46(24), 14299–14306. <https://doi.org/10.1029/2019GL085903>
- Čadek, O., Souček, O., Běhouňková, M., Choblet, G., Tobie, G., & Hron, J. (2019b). Long-term stability of Enceladus' uneven ice shell. *Icarus*, 319, 476–484. <https://doi.org/10.1016/j.icarus.2018.10.003>
- Čadek, O., Tobie, G., Van Hoolst, T., Massé, M., Choblet, G., Lefèvre, A., et al. (2016). Enceladus's internal ocean and ice shell constrained from Cassini gravity, shape, and libration data. *Geophysical Research Letters*, 43(11), 5653–5660. <https://doi.org/10.1002/2016GL068634>
- Chen, E., Nimmo, F., & Glatzmaier, G. (2014). Tidal heating in icy satellite oceans. *Icarus*, 229, 11–30. <https://doi.org/10.1016/j.icarus.2013.10.024>
- Choblet, G., Tobie, G., Sotin, C., Běhouňková, M., Čadek, O., Postberg, F., & Souček, O. (2017). Powering prolonged hydrothermal activity inside Enceladus. *Nature Astronomy*, 1(12), 841–847. <https://doi.org/10.1038/S41550-017-0289-8>
- Golle, O., Dumoulin, C., Choblet, G., & Čadek, O. (2012). Topography and geoid induced by a convecting mantle beneath an elastic lithosphere. *Geophysical Journal International*, 189(1), 55–72. <https://doi.org/10.1111/j.1365-246X.2012.05364.x>
- Hay, H. C., & Matsuyama, I. (2017). Numerically modelling tidal dissipation with bottom drag in the oceans of Titan and Enceladus. *Icarus*, 281, 342–356. <https://doi.org/10.1016/j.icarus.2016.09.022>
- Hay, H. C., & Matsuyama, I. (2019). Nonlinear tidal dissipation in the subsurface oceans of Enceladus and other icy satellites. *Icarus*, 319, 68–85. <https://doi.org/10.1016/j.icarus.2018.09.019>
- Hay, H. C., Trinh, A., & Matsuyama, I. (2020). Powering the Galilean satellites with moon-moon tides. *Geophysical Research Letters*, 47(15), e2020GL088317. <https://doi.org/10.1029/2020GL088317>
- Hemingway, D. J., & Mittal, T. (2019). Enceladus's ice shell structure as a window on internal heat production. *Icarus*, 332, 111–131. <https://doi.org/10.1016/j.icarus.2019.03.011>

- Hoolst, T. V., Baland, R.-M., & Trinh, A. (2016). The diurnal libration and interior structure of Enceladus. *Icarus*, 277, 311–318. <https://doi.org/10.1016/j.icarus.2016.05.025>
- Kang, W., Mittal, T., Bire, S., Campin, J.-M., & Marshall, J. (2022). How does salinity shape ocean circulation and ice geometry on Enceladus and other icy satellites? *Science Advances*, 8(29), eabm4665. <https://doi.org/10.1126/sciadv.abm4665>
- Kaula, W. M. (1964). Tidal dissipation by solid friction and the resulting orbital evolution. *Reviews of Geophysics*, 2(4), 661–685. <https://doi.org/10.1029/RG002i004p00661>
- Kvorka, J., & Čadek, O. (2022). A numerical model of convective heat transfer in Titan's subsurface ocean. *Icarus*, 376, 114853. <https://doi.org/10.1016/j.icarus.2021.114853>
- Lemasquerier, D., Grannan, A. M., Vidal, J., Cébron, D., Favier, B., Le Bars, M., & Aurnou, J. M. (2017). Libration-driven flows in ellipsoidal shells. *Journal of Geophysical Research: Planets*, 122(9), 1926–1950. <https://doi.org/10.1002/2017JE005340>
- Matsuyama, I. (2014). Tidal dissipation in the oceans of icy satellites. *Icarus*, 242, 11–18. <https://doi.org/10.1016/j.icarus.2014.07.005>
- Matsuyama, I., Beuthe, M., Hay, H. C., Nimmo, F., & Kamata, S. (2018). Ocean tidal heating in icy satellites with solid shells. *Icarus*, 312, 208–230. <https://doi.org/10.1016/j.icarus.2018.04.013>
- Nimmo, F., Barr, A. C., Běhouňková, M., McKinnon, W. B., & Dotson, R. (2018). The thermal and orbital evolution of Enceladus: Observational constraints and models. In P. M. Schenk, R. N. Clark, C. J. A. Howett, A. J. Verbiscer, & J. H. Waite (Eds.), *Enceladus and the icy moons of Saturn* (pp. 79–94). University of Arizona Press.
- Patočka, V., Čadek, O., & Martinec, Z. (2017). Energy balance of glacial isostatic adjustment: Importance of the rotational feedback. *Geophysical Journal International*, 212(2), 955–975. <https://doi.org/10.1093/gji/ggx469>
- Pope, S. B. (2000). *Turbulent flows*. Cambridge University Press.
- Rekier, J., Trinh, A., Triana, S. A., & Dehant, V. (2019). Internal energy dissipation in Enceladus's subsurface ocean from tides and libration and the role of inertial waves. *Journal of Geophysical Research: Planets*, 124(8), 2198–2212. <https://doi.org/10.1029/2019JE005988>
- Roberts, J. H. (2015). The fluffy core of Enceladus. *Icarus*, 258, 54–66. <https://doi.org/10.1016/j.icarus.2015.05.033>
- Rovira-Navarro, M., Gerkema, T., Maas, L. R., van der Wal, W., van Ostayen, R., & Vermeersen, B. (2020). Tides in subsurface oceans with meridional varying thickness. *Icarus*, 343, 113711. <https://doi.org/10.1016/j.icarus.2020.113711>
- Rovira-Navarro, M., Katz, R. F., Liao, Y., van der Wal, W., & Nimmo, F. (2022). The tides of Enceladus' porous core. *Journal of Geophysical Research: Planets*, 127(5), e2021JE007117. <https://doi.org/10.1029/2021JE007117>
- Rovira-Navarro, M., Matsuyama, I., & Hay, H. (2023). Thin-shell tidal dynamics of ocean worlds. *The Planetary Science Journal*, 23(2), 23. <https://doi.org/10.3847/PSJ/acae9a>
- Rovira-Navarro, M., Rieutord, M., Gerkema, T., Maas, L. R., van der Wal, W., & Vermeersen, B. (2019). Do tidally-generated inertial waves heat the subsurface oceans of Europa and Enceladus? *Icarus*, 321, 126–140. <https://doi.org/10.1016/j.icarus.2018.11.010>
- Soderlund, K. M. (2019). Ocean dynamics of outer solar system satellites. *Geophysical Research Letters*, 46(15), 8700–8710. <https://doi.org/10.1029/2018GL081880>
- Soderlund, K. M., Kalousová, K., Buffo, J. J., Glein, C. R., Goodman, J. C., Mitri, G., et al. (2020). Ice-ocean exchange processes in the Jovian and Saturnian satellites. *Space Science Reviews*, 216(5), 1–57. <https://doi.org/10.1007/s11214-020-00706-6>
- Souček, O., Běhouňková, M., Čadek, O., Hron, J., Tobie, G., & Choblet, G. (2019). Tidal dissipation in Enceladus' uneven, fractured ice shell. *Icarus*, 328, 218–231. <https://doi.org/10.1016/j.icarus.2019.02.012>
- Souček, O., Hron, J., Běhouňková, M., & Čadek, O. (2016). Effect of the tiger stripes on the deformation of Saturn's moon Enceladus. *Geophysical Research Letters*, 43(14), 7417–7423. <https://doi.org/10.1002/2016GL069415>
- Spencer, J. R., Nimmo, F., Ingersoll, A. P., Hurford, T. A., Kite, E. S., Rhoden, A. R., et al. (2018). Plume origins and plumbing: From ocean to surface. In P. M. Schenk, R. N. Clark, C. J. A. Howett, A. J. Verbiscer, & J. H. Waite (Eds.), *Enceladus and the icy moons of Saturn* (pp. 163–174). University of Arizona Press.
- Tajeddine, R., Rambaux, N., Lainey, V., Charnoz, S., Richard, A., Rivoldini, A., & Noyelles, B. (2014). Constraints on Mimas' interior from Cassini ISS libration measurements. *Science*, 346(6207), 322–324. <https://doi.org/10.1126/science.1255299>
- Thomas, P. C., Tajeddine, R., Tiscareno, M. S., Burns, J. A., Joseph, J., Lored, T. J., et al. (2016). Enceladus's measured physical libration requires a global subsurface ocean. *Icarus*, 264, 37–47. <https://doi.org/10.1016/j.icarus.2015.08.037>
- Tobie, G., Čadek, O., & Sotin, C. (2008). Solid tidal friction above a liquid water reservoir as the origin of the south pole hotspot on Enceladus. *Icarus*, 196(2), 642–652. <https://doi.org/10.1016/j.icarus.2008.03.008>
- Travis, B., & Schubert, G. (2015). Keeping Enceladus warm. *Icarus*, 250, 32–42. <https://doi.org/10.1016/j.icarus.2014.11.017>
- Tyler, R. (2008). Strong ocean tidal flow and heating on moons of the outer planets. *Nature*, 456(7223), 770–772. <https://doi.org/10.1038/nature07571>
- Tyler, R. (2009). Ocean tides heat Enceladus. *Geophysical Research Letters*, 36(15), 15205. <https://doi.org/10.1029/2009GL038300>
- Tyler, R. (2014). Comparative estimates of the heat generated by ocean tides on icy satellites in the outer solar system. *Icarus*, 243, 358–385. <https://doi.org/10.1016/j.icarus.2014.08.037>
- Tyler, R. (2020). Heating of Enceladus due to the dissipation of ocean tides. *Icarus*, 348, 113821. <https://doi.org/10.1016/j.icarus.2020.113821>
- Tyler, R., Henning, W. G., & Hamilton, C. W. (2015). Tidal heating in a magma ocean within Jupiter's moon Io. *The Astrophysical Journal - Supplement Series*, 218(2), 22. <https://doi.org/10.1088/0067-0049/218/2/22>
- Wilson, A., & Kerswell, R. R. (2018). Can libration maintain Enceladus's ocean? *Earth and Planetary Science Letters*, 500, 41–46. <https://doi.org/10.1016/j.epsl.2018.08.012>
- Zannoni, M., Hemingway, D., Gomez Casajus, L., & Tortora, P. (2020). The gravity field and interior structure of Dione. *Icarus*, 345, 113713. <https://doi.org/10.1016/j.icarus.2020.113713>